Molecular simulation of the separation of toluene and p-xylene with the thermally-robust ionic liquid triphenyl-p-phenyl sulfonyl phenyl phosphonium

Praveenkumar Sappidi[1], Brooks D. Rabideau[2], and C. Heath Turner[1,*]

[1]Department of Chemical and Biological Engineering, The University of Alabama, Tuscaloosa, AL 35487

[2]Department of Chemical & Biomolecular Engineering, University of South Alabama, Mobile, AL 36688

**Corresponding author contact information*

Phone: (205) 348-1733

Email: hturner@eng.ua.edu

Abstract

Here, we use molecular dynamics simulations to evaluate the behavior of toluene (TOL) and p-xylene (XYL) within three different solvents: *n*-hexane (HEX), *n*-heptane (HEP), and a thermally-robust ionic liquid (triphenyl-p-phenyl sulfonyl phenyl phosphonium + bis(trifluoromethylsulfonyl)imide (TPSP+Tf_2N)). Several different temperatures are explored, while the solvation structures, energetics, and dynamics of TOL and XYL are evaluated. The solvation free energy (ΔG_{solv}) and transfer free energy ($\Delta G_{transfer}$) of TOL and XYL are calculated using thermodynamic integration (TI). The transfer free energy of XYL from HEP/HEX to TPSP+Tf_2N is more favorable than that of TOL over the entire temperature range, while the transfer of both TOL and XYL becomes less favorable as the temperature increases. The diffusion rates of TOL and XYL are lower in the ionic liquid when compared to HEP and HEX, but the thermal stability of TPSP+Tf_2N may allow for higher operating temperatures and accelerated mass transport rates.

Keywords: Toluene; hexane; heptane; ionic liquids; molecular dynamics; free-energy

1. Introduction

Aromatic BTEX (benzene, toluene, ethylbenzene, and xylene) compounds are very important commodity chemicals that are used as raw materials for the polymer and plastics industry and in other chemical processes, and they are typically generated from petroleum refining operations. However, the energy-efficient separation of aromatic compounds, such as BTEX from hydrocarbon mixtures, is a major problem in the petroleum industry. The separation of BTEX from hydrocarbon mixtures is particularly challenging due to the formation of an azeotrope with the hydrocarbon mixture, providing a thermodynamic limit to traditional distillation processes. Several alternative separation techniques exist, such as azeotropic distillation, extractive distillation, and liquid-liquid extraction, but these methods are only effective when the BTEX concentration is above 20 wt% (Słomińska et al. 2013). In cases when the BTEX concentration is below 20 wt%, solvent-based extraction methods can play an important role (Domańska et al. 2007), due to their energy efficiency and industrial scalability. However, the selection of an effective solvent must satisfy a wide range of thermophysical and other environmental requirements, including high selectivity, low viscosity, high thermal stability, low toxicity, low cost, and high recycle potential.

Over the last couple of decades, the solvation and interfacial properties of ionic liquids have received a great deal of interest in a variety of applications. Examples include exfoliants for metal sulfates (Ludwig et al. 2015, Abedini et al. 2016, Atkinson et al. 2020), electrolytes for electric double-layer capacitors (Mahurin et al. 2016), adsorbents for metal ion separation (Liu et al. 2014), and as additives for enhancing the performance of gas separation membranes (Bara et al. 2007, 2008, Liu et al 2013, Shannon et al. 2015, Abedini et al. 2017, 2019, Flowers et al. 2017, Szala-Bilnik et al. 2019, 2020). In the past, various ammonium (Domańska et al. 2007), pyridium, and

imidazolium based (Matsumoto et al. 2004, Huang et al. 2004, Arce et al. 2007, Zhang et al. 2007, Larriba et al. 2013, 2014a, 2014b, 2015, Pena-Pereira and Namieśnik 2014), ionic liquids have been proposed for separating BTEX from hydrocarbon mixtures. For instance, Lorriba, et al. (Lorriba, et al. 2015) performed experiments using a binary ionic liquid mixture: 1-ethyl-4-methylpyridinium bis (trifluoromethanesulfonyl) imide ([4empy][Tf_2N]) and the 1-ethyl-3-methylimidazolium dicyanamide ([emim][DCA]), for separating BTEX from naphtha. They found that [4empy][Tf_2N] and [emim][DCA] are potential candidates when the BTEX concentration in naphtha is below 20 wt% (Lorriba, et al. 2015). However, the commercialization of these specific ionic liquids for large scale applications is impractical, due to their toxicity and high raw material cost. Mulyono, et al. (Mulyono et al. 2014) performed experiments using the deep eutectic solvent (DES) tetrabutylammonium bromide + sulfolane for the separation of BTEX from n-octane, where sulfolone acts as a complexing agent with the aromatics. Interestingly, they found that sulfolane is absent in the raffinate phase, thus indicating that the tetrabutylammonium bromide + sulfolane can be potentially be used for the separation of BTEX (Mulyono et al. 2014). However, a common practical limitation to the industrial application of all of these previous ionic liquids is that they are not stable at elevated temperatures, with most of them decomposing near 250 ^{o}C (Maton et al. 2013).

Recently, (Benchea et al. 2017) developed more thermally-stable ionic liquids based on tetraphenyl phophonium (TPP^{+}) and triphenyl sulfonium (TPS^{+}) species. Rabideau, et al. (Rabideau et al. 2018) performed experiments and computational studies of these ILs, and they showed that the incorporation of aromatic compounds (such as peraryl) on the ionic species provides higher thermal stability (up to 300 ^{o}C), while also possessing higher heat capacity and low volatility. Cassity, et al. (Cassity et al. 2017) performed thermogravimetric analysis and

molecular dynamics simulations on a tetra aryl phosphonium cation along with a bis (trifluoromethane) sulphonamide anion, and they were able to demonstrate excellent thermal stability up to 300 ^{o}C for a duration of three months. Furthermore, it has been observed that the thermal stability is not compromised by modifying the cation ligands (e.g., phenoxy, phenyl acyl, or phenyl sulphonyl) on these peraryl-based ILs (Cassity et al. 2017). Recently, Odugbesi, et al. (Odugbesi et al. 2019) performed chromatography experiments using sulfonium and phosphonium-based ILs in the column as the stationary phase for separating polyaromatic hydrocarbons and polychlorinated biphenyls. These sulfonium- and phophonium-based ILs showed high selectivity for the aromatic components and excellent thermal stability, and thus, demonstrate the potential for separating BTEX from hydrocarbon mixtures (Odugbesi et al. 2019).

Despite all the above studies, there are no reports in the literature that have been focused on the molecular-level characteristics of these thermally-stable ILs for the separation of BTEX from hydrocarbon mixtures. Here, we use all-atom molecular dynamics (MD) simulations to uncover the molecular-level behavior of these thermally-robust ILs for BTEX separation applications. Accordingly, we model the structure and dynamics of toluene (TOL) and *p*-xylene (XYL) in *n*-hexane (HEX), *n*-heptane (HEP), and an IL composed of triphenyl-p-phenylsulfonyl phenyl phosphonium (TPSP) cation and bis (trifluoromethane) sulfonimide (Tf_2N) anion. The overall thermodynamics of the aromatic extraction for a potential liquid-liquid extraction process is evaluated using the solvation free energy (ΔG_{solv}) and the transfer free energy ($\Delta G_{transfer}$), and the effect of temperature on these quantities is quantified. Furthermore, the transfer free energy is translated into a partition coefficient (log *P*) for more directly evaluating the separation performance for liquid-liquid extraction. These calculations are expected to provide benchmark thermodynamic values for interpreting the experimental performance characteristics, and they

serve as a guide for future computational investigations of the thermophysical properties of these thermally-robust IL solvents for other applications.

2. Methodology and Simulation Details

In order to assign partial charges for the TPSP force field used in the molecular dynamics simulations, electronic structure calculations were first performed on an isolated TPSP molecule in the gas phase. The initial geometry optimization and subsequent calculation of partial charges were estimated using the ChelpG (Chirlian et al. 1987) scheme using density functional theory calculations within Gaussian16 (Frisch et al. 2016) with the B3LYP (Stephens et al. 1994) functional and the 6-31G (d,p) basis set. The surface electrostatic potential map is calculated by mapping electrostatic potential on to the surface of the constant electron density evaluated by using the total SCF density. Similar geometry optimizations and charge calculations were performed for TOL, XYL, HEX and HEP. Although scaled charges have been frequently used by others to account for polarizability when modelling ionic liquids (Lisal et al. 2014, Zhang et al. 2015), we used the full (integer) charge values. Recently, it has been shown by Cui et al. 2019 that charge scaling can underestimate the solvation free energy of multi-component solutions (similar to our current systems), so we opted for integer charges on our cation and anion molecules. The resulting partial atomic charges are summarized in Table S1 and S2 in the Supporting Information (SI). Figure 1 presents the optimized molecular structure of TPSP, as well as a visualization of the surface electrostatic potential.

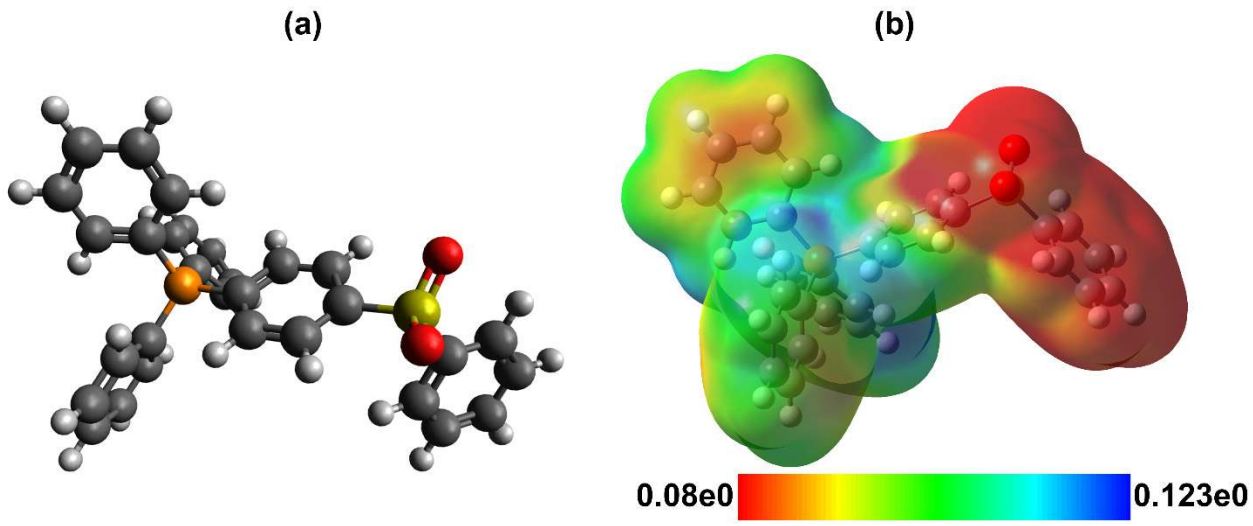

Figure 1. (a) Optimized molecular structures of TPSP, (b) TPSP along with surface electrostatic potential (au). Colour codes: grey-carbon, white-hydrogen, orange-phosphorous, yellow-sulfur, red-oxygen.

All of the MD simulations were performed using GROMACS 2019.4 (Lindahl et al. 2019), and the OPLS (Jorgensen et al. 1996) all-atom force field was used to represent all of the bonded and non-bonded interactions. The particle mesh Ewald (PME) (Darden et al. 1993) method is used for calculating the electrostatic interaction energies, and the Lennard-Jones potential is used for calculating the van der Waals interactions. A cut-off radius of 1.2 nm is used for both the dispersion and electrostatic interactions. The temperature and pressure were maintained using the Nosé-Hoover thermostat and the Parrinello-Rahman barostat, respectively, each with a time constant of 5 ps. The leap-frog algorithm is used for solving the equation of motion with a 2 fs time step, while all bond lengths were constrained using LINCS method (Hess et al. 1997).

A cubic box with initial dimensions of $6\times6\times6$ nm^3 was used for all simulations. Three different solvent systems were modeled, corresponding to: (1) 620 molecules of HEP; (2) 620 molecules of HEX; and (3) 150 TPSP ions + 150 Tf_2N ions. Following energy minimization using the steepest

descent method, all three simulation systems were simulated using MD for a total duration of 20 ns at a temperature of 300 K and a pressure of 1 bar in the isothermal-isobaric (NPT) ensemble. Following equilibration, 20 molecules of TOL and 20 molecules of XYL were added randomly to each of the solvent systems. This concentration provides for good sampling statistics, while still maintaining a relatively dilute concentration. The composition details of each simulated system and the equilibrated density values are summarized in Table 1. The simulated densities of HEP and HEX fall within 3% of the experimental values (Dymond et al. 1980, 1988).

Table 1. The number of molecules in each simulation system, equilibrated density (ρ) and experimental density at 300 K and 1 bar. The standard deviation values are given in parenthesis.

solvent	**number of molecules**			**density of solvent ρ (kg/m^3)**		
	solvent	**TOL**	**XYL**	**current simulation**	**experiment**	**previous simulation**
pure solvent system						
HEP	620	0	0	679.42 (1.8)	679.6 (Dymond et al. 1988)	679.7 (Wu et al. 2009)
HEX	620	0	0	661.44 (1.6)	655.0 (Dymond et al. 1980)	658.0 (Patel and Brooks III 2006)
TPSP+ Tf_2N	150+150	0	0	1241.72 (30.3)		
TOL mixed system						
HEP	620	20	0	676.20 (3.7)		
HEX	620	20	0	637.03 (1.6)		
TPSP+ Tf_2N	150+150	20	0	1234.91 (26.0)		
XYL mixed system						
HEP	620	0	20	677.91 (2.7)		
HEX	620	0	20	638.94 (2.2)		
TPSP+ Tf_2N	150+150	0	20	1239.57 (41.7)		

Figure 2 presents the initial simulation snapshots of TOL and XYL in HEP, HEX, and TPSP+Tf_2N. All six systems were simulated at four different temperatures: 300 K, 340 K, 380 K, and 420 K, in order to evaluate the solvation characteristics over a range of conditions. All of these simulations were performed for a total of 20 ns simulation time, and the analysis was

performed on the last 5 ns of the trajectory. Standard deviations of the average values are calculated by subdividing the 5 ns production stage into 5 independent blocks.

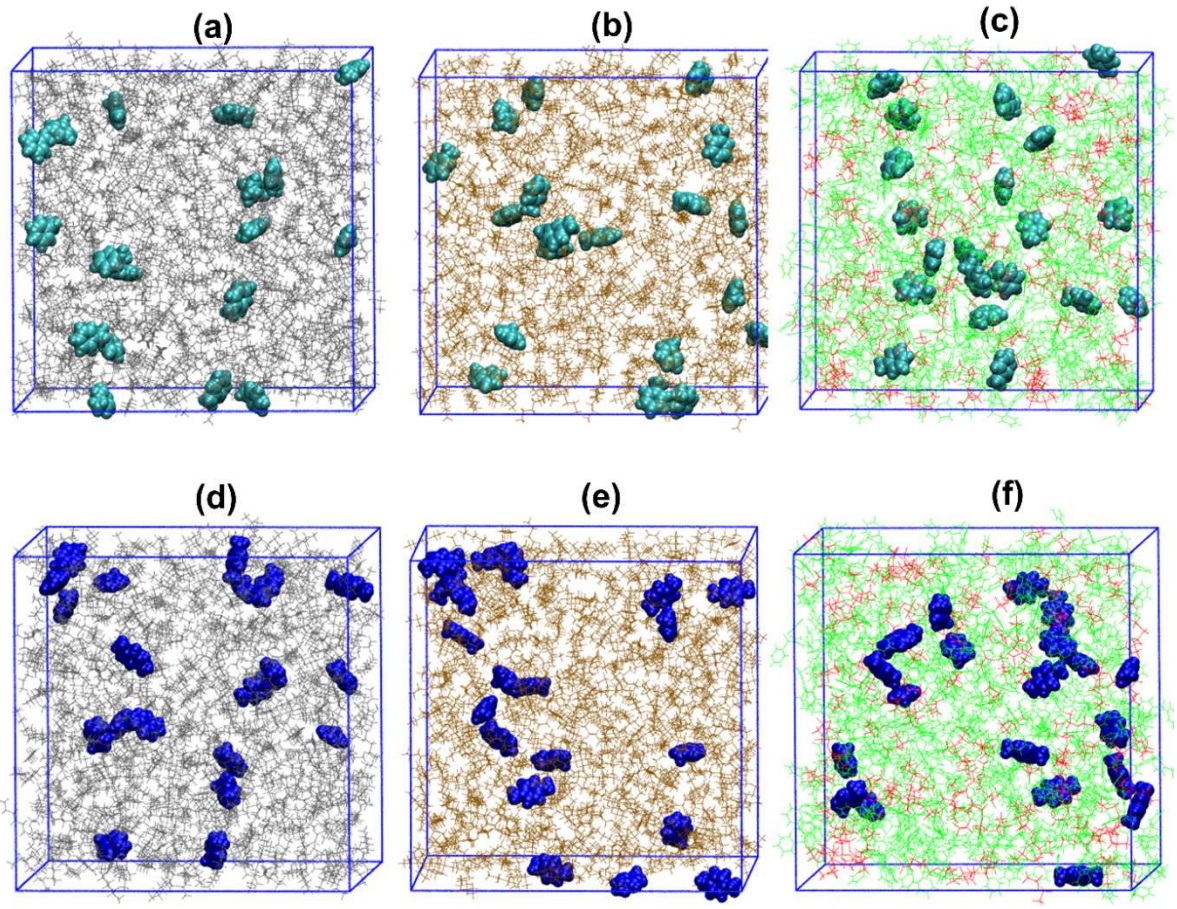

Figure 2. Initial simulation snapshots for TOL in (a) HEP, (b) HEX and (c) TPSP+Tf_2N. Similarly, XYL in (d) HEP, (e) HEX and (f) TPSP+ Tf_2N. Colour codes: cyan-TOL, blue-XYL, grey-HEP, brown-HEX, green-TPSP and red-Tf_2N.

In order to calculate the solvation free energy (ΔG_{solv}) of TOL and XYL, a two-stage thermodynamic integration procedure is used (Shirts et al. 2003, Sappidi et al. 2018). According to this approach, ΔG_{solv} can be described as:

$$G_{solv} = \Delta G_{vdw} + \Delta G_{ele} \quad (1)$$

This can be further expanded as:

$$\Delta G_{Solv} = \int_{\lambda_{vdw}=0,\lambda_{ele}=0}^{\lambda_{vdw}=1,\lambda_{ele}=0} \left\langle \frac{\partial U(\lambda)}{\partial \lambda} \right\rangle_{\lambda} d\lambda + \int_{\lambda_{vdw}=1,\lambda_{ele}=0}^{\lambda_{vdw}=1,\lambda_{ele}=1} \left\langle \frac{\partial U(\lambda)}{\partial \lambda} \right\rangle_{\lambda} d\lambda \qquad (2)$$

where λ_{ele} and λ_{vdw} represent the coupling constants for Coulomb and van der Waals interactions, respectively. The λ parameter is used to modulate the non-bonded potential component of the Hamiltonian using the linear relationship:

$$U(\lambda) = \lambda\, U_F + (1 - \lambda)\, U_I \qquad (3)$$

Here, U_F and U_I are the total configurational energies of final and initial states, respectively. The expressions for individual non-bonded (electrostatics and van der Waals) potential components due to variations of λ are provided in earlier reports (Shirts et al. 2003, Sappidi et al. 2018). The first stage is used to calculate ΔG_{vdw}. Here, we grow one TOL (or XYL) from the initial state represented as $\lambda_{vdw} = 0$ and $\lambda_{ele} = 0$ (i.e., there is no interaction) to a state with full van der Waals interaction but without Coulomb interaction (i.e., $\lambda_{vdw} = 1$ and $\lambda_{ele} = 0$). The second stage is used to calculate ΔG_{ele}. Here, we grow the interactions from $\lambda_{vdw} = 1$ and $\lambda_{ele} = 0$ to the state with full van der Waals and Columbic interactions (i.e., $\lambda_{vdw} = 1$ and $\lambda_{ele} = 1$). We avoid issues related to divergence by taking many intermediate points along the thermodynamic integration path. We calculate $\langle \partial U/\partial \lambda \rangle$ at different values of the coupling parameters λ_{vdw} and λ_{ele}, which were incremented in steps of 0.05 in the range 0.0 to 1.0. Thus, we performed 21 simulations for ΔG_{vdw} and 21 simulations for ΔG_{ele} in order to calculate the value of the solvation free-energy of each data point reported.

The transfer free energy ($\Delta G_{transfer}$) (Bannan et al. 2016) is evaluated by directly using the free-energy difference of the aromatics between the HC phase and the IL phase, according to the following expression:

$$\Delta G_{transfer} = (\Delta G_{Solv})_{IL} - (\Delta G_{Solv})_{HC} \quad (4)$$

The partition coefficient (log *P*) is then calculated using the expression: [45]

$$\log P = -\frac{\Delta G_{transfer}}{2.303RT} \quad (5)$$

Here, R is the ideal gas constant and T is the temperature.

Finally, the self-diffusion coefficients of TOL and XYL are calculated by applying the Einstein relation to the linear regime of the mean-squared displacement of the molecular trajectories.

3. Results and Discussion

3.1. TOL and XYL Structure in HEP, HEX, and TPSP

The structural properties of our mixtures are investigated by calculating the inter and intramolecular radial distribution functions (RDFs) of key sites in our systems. Figure 3 (a-d) illustrates the RDF between the aliphatic carbon (C_{ALI}) of TOL with different carbon sites of the solvent molecules. Similarly, Figure 3 (e-h) illustrates the RDF between the aromatic carbons (C_{ARO}) of TOL with different carbon sites of the solvent molecules. The first peak is located at ~0.41 nm for C_{ALI}-C_{HEP}, ~0.42 nm for C_{ALI}-C_{HEX}, ~0.57 for C_{ALI}-C_{TPSP} (atoms near the S), but only a very small peak is found for C_{ALI}-C_{TPSP} (atoms near the P), located at ~0.54 nm. Similarly,

a first small peak is located at ~0.52 nm for C_{ARO}-C_{HEP}, ~0.52 nm for C_{ARO}-C_{HEP}, ~0.63 nm for C_{ARO}-C_{TPSP} (atoms near the S), and ~0.67 nm for C_{ARO}-C_{TPSP} (atoms near the P). As expected, the intensities of the peaks show a decrease with an increase in temperature. In comparison, the aliphatic carbon of TOL shows a stronger propensity than the aromatic carbons to interact with the carbon atoms of HEP, HEX, and TPSP. This behavior and the peak positions are in good agreement with the computational work of (Celia-Silva et al. 2020) where the aliphatic carbon atoms of TOL show strong interaction with the terminal carbon atoms of asphaltenes.

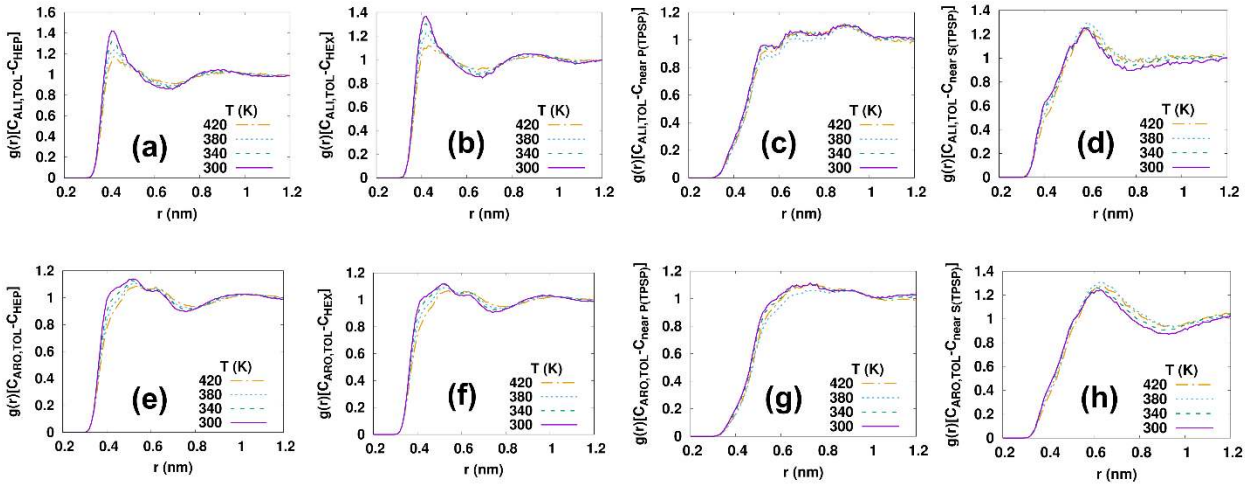

Figure 3. RDF plots of the aliphatic carbon (C_{ALI}) of toluene with the carbon atoms of the solvents: (a) terminal carbon atom of HEP; (b) terminal carbon atom of HEX; (c) carbon atoms near the P of TPSP; and (d) carbon atoms near the S of TPSP. Similarly, the RDF plots of the aromatic carbons (C_{ARO}) of toluene with the carbon atoms of the solvents: (e) terminal carbon atom of HEP; (f) terminal carbon atom of HEX; (g) carbon atoms near the P of TPSP; and (h) carbon atoms near the S of TPSP.

Similarly, Figure 4 shows the RDF plot between (C_{ALI}) and (C_{ARO}) of XYL with the carbon atoms of HEP, HEX, and TPSP. The first peak is located at ~0.41 nm for C_{ALI}-C_{HEP}, ~0.41 nm for C_{ALI}-C_{HEX}, ~0.57 nm for C_{ALI}-C_{TPSP} (atoms near the S), ~0.54 nm for C_{ALI}-C_{TPSP} (atoms near the P), ~0.52 nm for C_{ARO}-C_{HEP}, ~0.52 nm for C_{ARO}-C_{HEX}, ~0.61 nm for C_{ARO}-C_{TPSP} (atoms near the S), and there is no peak evident for C_{ARO}-C_{TPSP} (atoms near the P). The aliphatic carbon of XYL

shows moderately stronger interaction with the carbon atoms of HEP and HEX than the aromatic carbon, while both of the XYL carbon interactions with the TPSP carbon sites are relatively weak. Furthermore, it is evident from the Figures 3 and 4 that the C_{ALI} interacts more with the carbon atoms near the S on TPSP versus the carbon atoms near the P on the TPSP, due to the partial negative charge near the S (as seen in Figure 1(b)). In addition, we have calculated the RDFs between (C_{ALI} , C_{ARO}) of TOL and XYL with the central carbon atoms of HEX and HEP (Figure S1). We do not see a significant peak for the central carbon atoms on HEX and HEP with either C_{ALI} or C_{ARO}. From all of these RDF curves, we can clearly see that TOL and XYL tend to reside near the terminal carbon atoms of HEX and HEP.

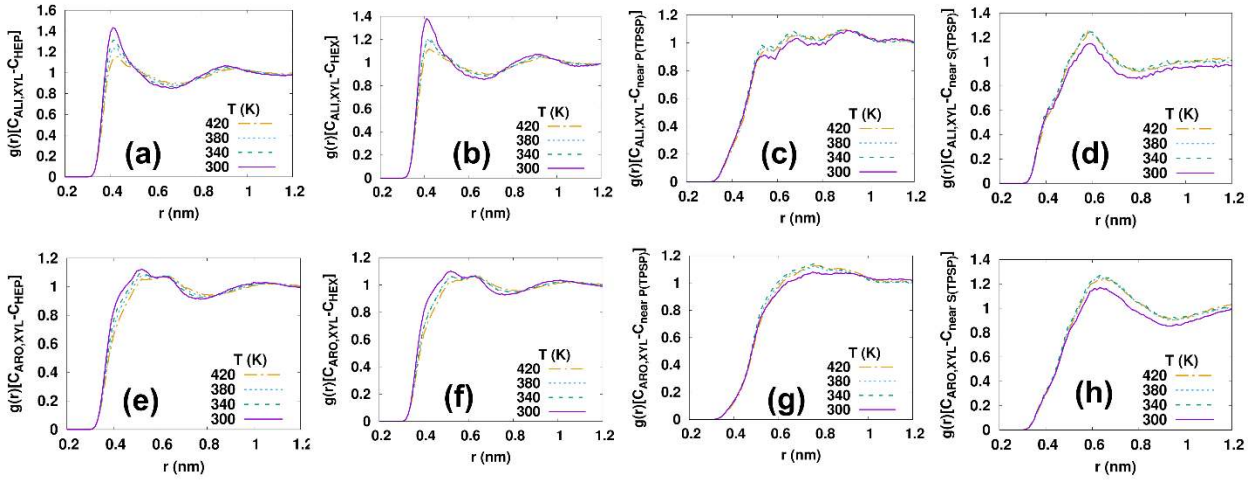

Figure 4. RDF plots of the aliphatic carbons (C_{ALI}) of XYL with: (a) terminal carbon atom of HEP; (b) terminal carbon atom of HEX; (c) carbon atoms near the P of TPSP; (d) carbon atoms near the S of TPSP. Similarly, the RDF plots of the aromatic carbons (C_{ARO}) of toluene with the carbon atoms of the other solvents: (e) terminal carbon atom of HEP; (f) terminal carbon atom of HEX; (g) carbon atoms near the P of TPSP; and (h) carbon atoms near the S of TPSP.

Additional analyses of other site-site radial distribution functions are shown in Figure S3 and S4, including the interactions of C_{ALI} and C_{ARO} of TOL and XYL with the oxygen (O_{TPSP}), phosphorous (P_{TPSP}), and sulfur (S_{TPSP}) atoms of TPSP. For both TOL and XYL, the first peaks are found at distances of ~0.35 nm for C_{ALI}-O_{TPSP}, ~0.58 nm for C_{ALI}-P_{TPSP}, and ~0.43 nm for

C_{ALI}-STPSP, while the peaks corresponding to C_{ARO} with O_{TPSP}, P_{TPSP}, and S_{TPSP} and negligible, indicating very weak interaction. Similarly, Figures S5 and S6 show the radial distribution functions of C_{ALI} and C_{ARO} of TOL and XYL with the carbon (C_{Tf2N}), fluorine (F_{Tf2N}), and oxygen (O_{Tf2N}) atoms of Tf_2N. For both TOL and XYL, the first peak is located at ~0.41 nm for C_{ALI}-C_{Tf2N}, ~0.35 nm for C_{ALI}-F_{Tf2N} and ~0.38 for C_{ALI}-O_{Tf2N}. Again, no significant peak is seen for C_{ARO} with C_{Tf2N}, F_{Tf2N}, or O_{Tf2N}, indicating very weak interactions with these sites. In conclusion, we find that the aliphatic carbon atoms of TOL and XYL show much stronger interaction with the atoms (O, P and S) of TPSP and (C, F, and O) Tf_2N.

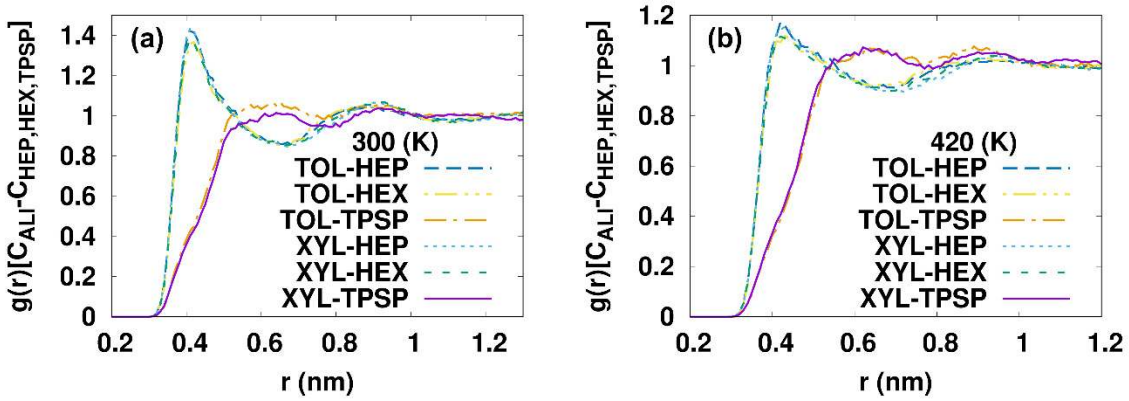

Figure 5. RDF plot of the aliphatic carbon (C_{ALI}) of (TOL and XYL) with the terminal carbon atoms of HEP and HEX, and the carbon atoms near the P, S of TPSP for: (a) 300 K; and (b) 420 K.

Figure 5 presents a comparison of the RDFs of C_{ALI} of TOL and XYL with the terminal carbon atom of HEP, terminal carbon atom of HEX, and the carbon atoms near the P, S of TPSP at temperatures of 300 K and 420 K. For both TOL and XYL, significant peaks are seen for the C_{ALI}-C_{HEP} and C_{ALI}-C_{HEX} when compared to C_{ALI}-C_{TPSP}. If we compare the preferred TOL and XYL locations on the TPSP, we see a more pronounced peak with carbon atoms near S when compared to carbon atoms near P (see Figure 3 (d,h) and Figure 4 (d, h)). However, we observe significant interactions of C_{ALI} (TOL and XYL) with the other non-carbon sites on TPSP and Tf_2N. These

results clearly indicate a slight dispersive interaction between aliphatic carbon atoms of TOL and XYL with terminal carbon atoms of HEX, HEP and carbon atoms near the P, S and of TPSP. In general, there are only very weak interactions between the aromatic carbon atoms of TOL and XYL with the carbon atoms of HEX, HEP, and TPSP.

3.3. Diffusion of Toluene and Xylene

In Figure 6, the self-diffusion coefficients (D) of TOL and XYL are shown, corresponding to the different solvents (HEX, HEP, and TPSP+Tf_2N) at several different temperatures. The mean-squared displacement (MSD) data used to extract these values are included in Figure S7 of the Supporting Information. It is found that the diffusion of TOL and XYL is much higher (~20×) in HEP and HEX than in TPSP+Tf_2N, and this is not surprising due to the higher viscosities typically found for ionic liquids. There is moderate diffusion selectivity observed in the HEP and HEX solvents (depending upon the temperature), but very little diffusion selectivity found in the TPSP+Tf_2N solvent. However, due to the increased thermal stability of the TPSP+Tf_2N, there is the potential to mitigate the slow transport behavior in the IL with increased operational temperature.

The diffusive behavior is further evaluated by calculating the van Hove (Kim and Mattice 2002) space time correlation (see the Figure S8), which we use to quantify the probability of our solute displacement (TOL and XYL) by a distance 'r' during the time interval 't'. The van Hove correlation function peaks naturally shift to larger 'r' values with increase in time. At t = 200 ps, the peak positions of TOL and XYL correspond to ~2 nm in HEX and HEP, but these peaks are closer to ~0.5 nm in the TPSP+Tf_2N solvent. These data correspond to the lowest temperature (T = 300 K) simulated in our work, so they represent a lower bound to the system dynamics expected at the higher temperatures. Overall, this dynamic information confirms the significant diffusion

attenuation found in the TPSP+Tf_2N solvent, but the data also provides additional verification that the MD trajectories are sufficiently long for obtaining representative diffusion statistics.

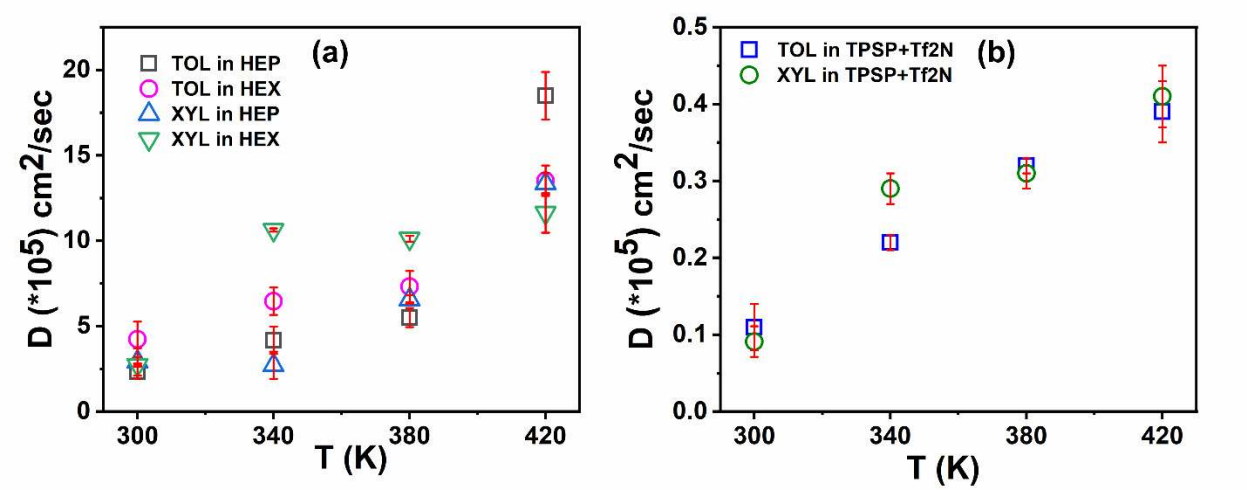

Figure 6. Diffusion of TOL and XYL as function of temperature. The error bars represent the standard deviations.

The D values of TOL and XYL at two extreme temperatures are provided in Table 2. The D values of TOL and XYL predicted here are similar to earlier studies (Kim and Lee 2002, Köhler and Müller 1995). The D value of TOL at 300 K is 4.23×10^{-5} cm^2/sec in HEX and this is in good agreement with experimental observations, corresponding to 3.46×10^{-5} cm^2/sec at 23 °C (Köhler and Müller 1995).

Table 2. Self-diffusion coefficient values of TOL and XYL at 300 K and 420 K. The standard deviation values are shown in parenthesis.

Solvent	D_{TOL} ($\times10^{-5}$ cm^2/sec)		D_{XYL} ($\times10^{-5}$ cm^2/sec)	
	300 K	**420 K**	**300 K**	**420 K**
HEP	2.32 (0.4)	18.49 (1.4)	2.91 (0.4)	13.35 (0.6)
HEX	4.23 (0.8)	13.51 (0.9)	2.72 (0.1)	11.63 (0.9)
TPSP+Tf_2N	0.11 (0.03)	0.39 (0.04)	0.09 (0.01)	0.41 (0.04)

3.4. Solvation and Transfer Free-Energy of Toluene and Xylene

Figure 7 presents the thermodynamic behavior of the solvation free energy of TOL due to variations in the coupling parameter (λ_{ele} and λ_{vdw}) in different solvents. It is observed from Figure

9 that the van der Waals interaction shows a favorable contribution to the total solvation free energy (more negative ΔG_{solv}) of TOL over the entire range of temperatures 300 K < T < 420 K. More favorable solvation is also seen in the ionic liquid (TPSP+Tf_2N), as compared to HEP and HEX. However, with an increase in temperature, ΔG_{solv} becomes unfavorable in all three solvents HEP, HEX, and TPSP+Tf_2N.

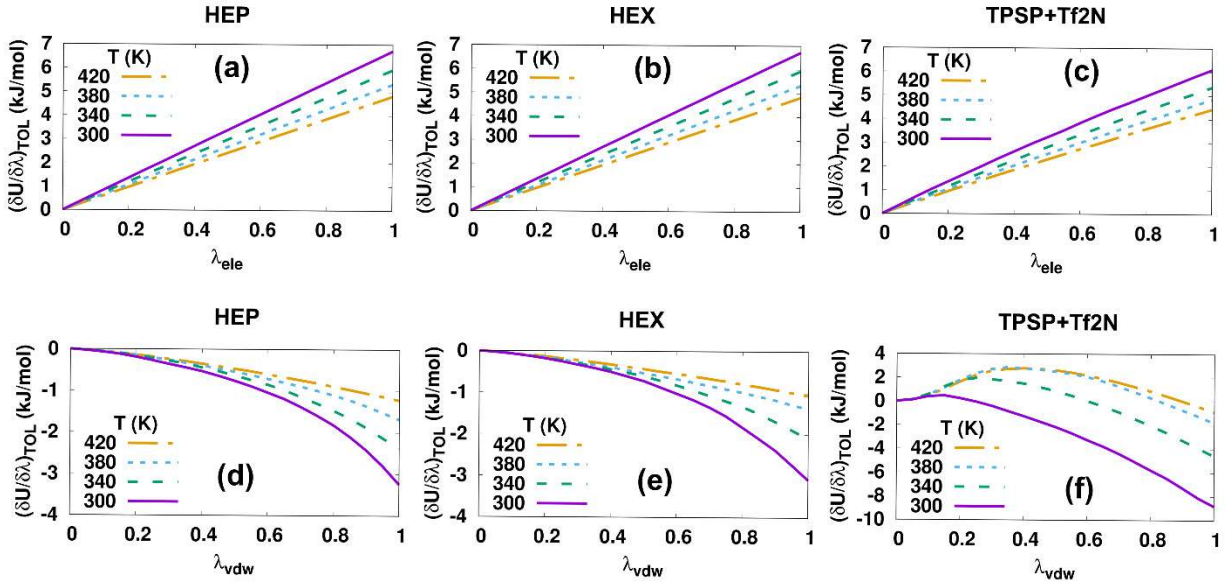

Figure 7. The $\langle \partial U/\partial \lambda \rangle$ of TOL as a function of the coupling parameter (λ_{ele} and λ_{vdw}). The ΔG_{solv} contribution due to the electrostatic coupling is shown in: (a) HEP; (b) HEX; and (c) TPSP+Tf_2N. Similarly, the contribution due to van der Waals coupling is shown in: (d) HEP; (e) HEX; and (f) TPSP+Tf_2N.

Similarly, Figure 8 presents the thermodynamic behavior of the solvation free energy of XYL due to the variation of the coupling parameter in different solvents. We see that the favorable contributions to the total solvation free energy are dominated by electrostatic interactions. The solvation of XYL is much stronger in TPSP+Tf_2N when compared to HEP and HEX, but the solvation ultimately becomes unfavorable with an increase in temperature. We see that the electrostatic interaction of XYL with the solvent molecules is more favorable, as compared to the solvation of TOL. Fundamentally, the presence of the methyl group on the TOL leads to a larger

polarizability and dipole moment, which leads to stronger electrostatic repulsion in the different solvents, especially the TPSP+Tf_2N (Grissom et al. 2018).

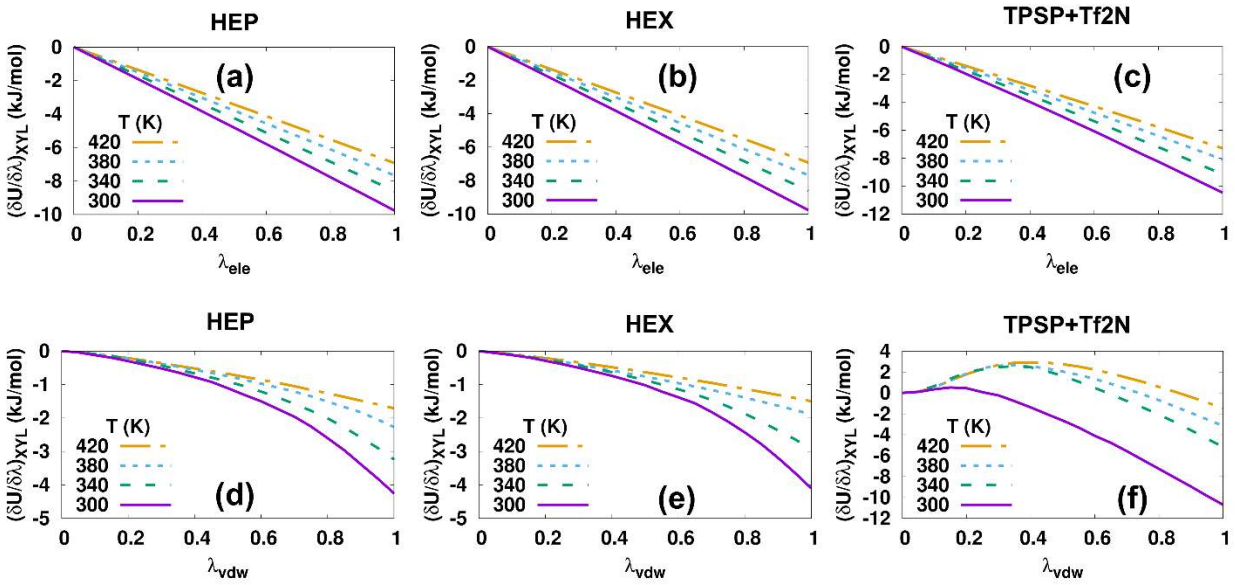

Figure 8. The $\langle \partial U/\partial \lambda \rangle$ of XYL as a function of the coupling parameter (λ_{ele} and λ_{vdw}). The ΔG_{solv} contribution due to electrostatic decoupling is shown in: (a) HEP, (b) HEX, and (c) TPSP+Tf_2N. Similarly, the contribution due to van der Waals decoupling is shown in: (d) HEP, (e) HEX, and (f) TPSP+Tf_2N.

Figure 9 presents the solvation free energy (ΔG_{solv}) of TOL and XYL as a function of temperature. The ΔG_{solv} in the ionic liquid (TPSP+Tf_2N) is much more thermodynamically favored when compared to HEP and HEX over the entire range of temperature (300 K < T < 420 K), but the ΔG_{solv} of both solutes becomes unfavorable with an increase in temperature.

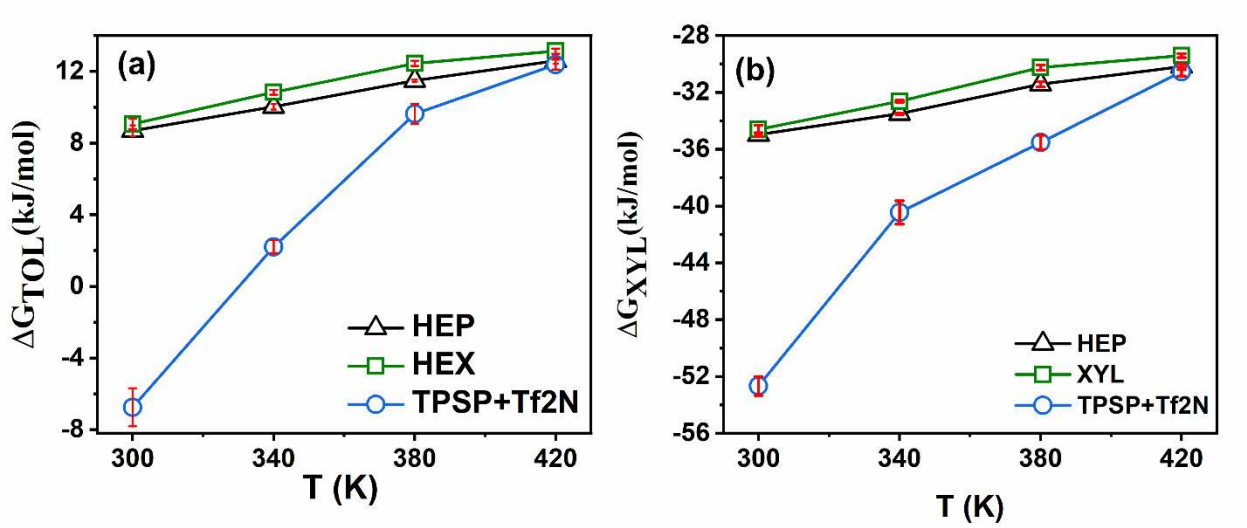

Figure 9. Total solvation free energy (ΔG_{solv}) as a function of temperature: (a) TOL; and (b) XYL. The error bars represent the standard deviations.

The $\Delta G_{transfer}$ is useful for estimating the efficiency of aromatic extraction from a HC solution to an IL solution using a liquid-liquid extraction process, and our calculated results are shown in Figure 10. The $\Delta G_{transfer}$ value becomes less negative with an increase in temperature from 300 K to 420 K. It is evident from Figure 10 that the solute transfer (TOL, XYL) from the organic phase (HEP, HEX) to the ionic liquid (TPSP+Tf_2N) is highly favorable at 300 K and less favorable at 420 K. Moreover, at all temperatures, it is observed that the transfer of XYL from HEP/HEX to TPSP+Tf_2N is more favorable when compared to the transfer of TOL. As the temperature is increased from 300 K to 420 K, the $\Delta G_{transfer}$ of TOL from HEP to TPSP+Tf_2N decreases by 98%, and it decreases by 95% from HEX to TPSP+Tf_2N. Similarly, the $\Delta G_{transfer}$ of XYL from HEP to TPSP+Tf_2N decreases by 97%, and it decreases by 93% from HEX to TPSP+Tf_2N. Overall, $\Delta G_{transfer}$ follows the general order: $XYL_{HEX} < XYL_{HEP} < TOL_{HEX} < TOL_{HEP}$ at 300 K.

Our simulation predictions also need to be understood within the context of the experimental phase behavior. It is known that the experimental melting temperature of pure TPSP+Tf_2N is 416

K (Rabideau et al. 2018). However, it is expected that the presence of the hydrocarbon species (TOL and XYL) would lower the melting temperature of overall solution, and it is most likely that these solutions would be liquids within the temperature ranges simulated.

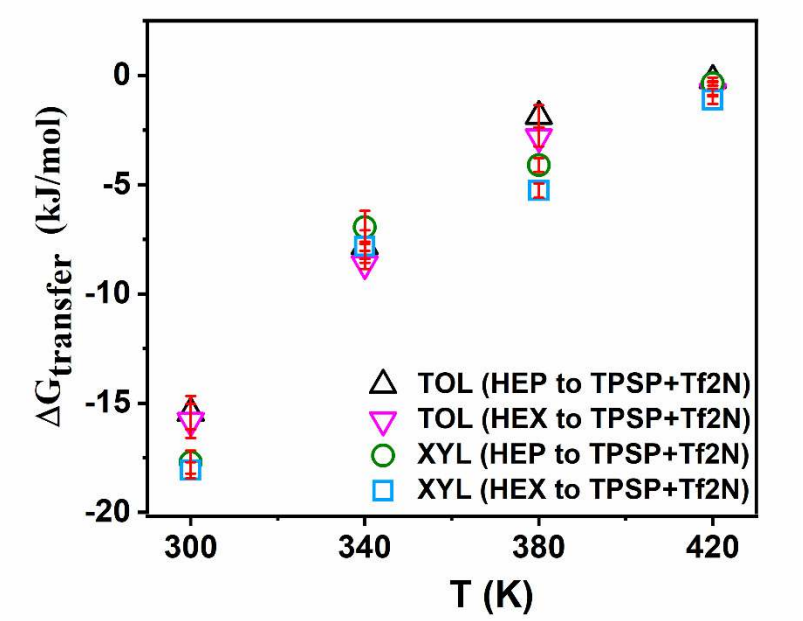

Figure 10. Transfer free energy ($\Delta G_{transfer}$) of TOL and XYL from an organic solvent (HEP, HEX) to the ionic liquid (TPSP+Tf_2N) as a function of temperature. The error bars represent the standard deviations.

3.5. Partition Coefficient of Toluene and Xylene

Figure 11 presents the partition coefficients (log *P*) as a function of temperature. The log *P* values of TOL and XYL show a decrease with an increase in temperature. As the temperature increases from 300 K to 420 K, the log *P* of TOL shows a 127% decrease for HEP to TPSP+Tf_2N and a 95% decrease for HEX to TPSP+Tf_2N. Similarly, the log *P* of XYL shows a 98% decrease for HEP to TPSP+Tf_2N and a 93% decrease for HEX to TPSP+Tf_2N. The partition coefficient values from our simulation results are approximately ten-fold higher for TOL and XYL than in the imidazolium-based ionic liquids from the gas (CO_2 and N_2) phase (Cichowska-Kopczyńska et al. 2018, Hiraga et al. 2016). The experimental log *P* values for TOL in imidazolium [Tf_2N] ionic

liquids vary within 0.05-0.20 in the temperature range from 280 K to 310 K (Cichowska-Kopczyńska et al. 2018). Similarly, the partition coefficient values for XYL in (1-butyl-3-methylimidazolium [Tf_2N] fall around 0.2 at 353 K and 6 MPa (Cichowska-Kopczyńska et al. 2018). Overall, the log *P* values follow the sequence of $XYL_{HEX} < XYL_{HEP} < TOL_{HEX} < TOL_{HEP}$ at 300 K. Thus, our molecular simulation data suggests that TPSP+Tf_2N can be effective for extracting toluene and p-xylene from hydrocarbon mixtures at room temperature.

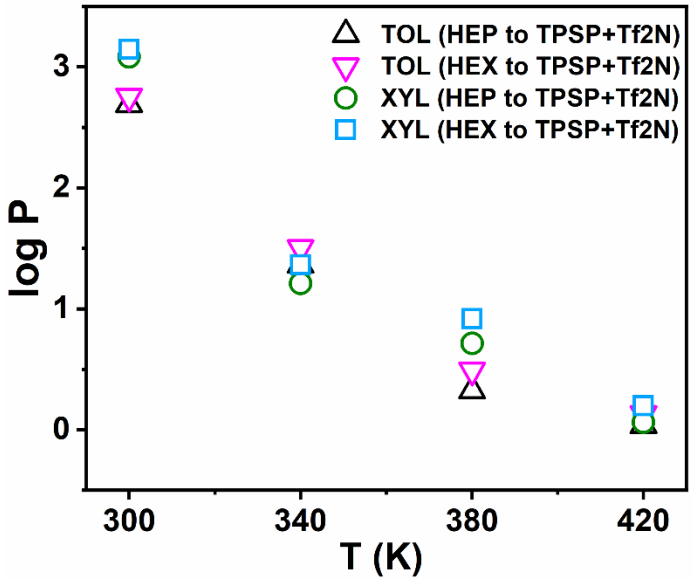

Figure 11. Partition coefficient (log *P*) of TOL and XYL as a function of temperature.

4. Conclusion

All-atom MD simulations have been used to quantify the molecular-level separation characteristic of TOL and XYL in three different solvents: HEX, HEP, and TPSP+Tf_2N. In particular, our results reveal important thermodynamic and solvation properties of the thermally-robust ionic liquid TPSP+Tf_2N. We find that the aliphatic carbons of TOL and XYL have a stronger interaction with the carbon atoms near the P, S of TPSP. Also, it is observed that TOL and XYL have a stronger solvation in TPSP+Tf_2N (compared to HEP and HEX), and this can be attributed to stronger partial charges on P, S, and O. The transfer free energy of XYL from

HEP/HEX to TPSP+Tf_2N is more favorable than that of TOL over the entire temperature range, while the transfer of both TOL and XYL becomes less favorable as the temperature increases from 300 K to 420 K. Although the solvation of TOL and XYL is very high in the TPSP+Tf_2N solvent, the diffusion rates of these species are approximately twenty times lower when compared to the diffusion in HEP and HEX. Overall, this selectivity and diffusion behavior can be important for designing solvent-based separation processes, and the thermal stability of TPSP+Tf_2N enables broader operating ranges, which could be used to counteract the slower diffusion behavior that is characteristic of most ILs.

Supplementary Information

Supporting Information is available: The partial atomic charges, additional RDF plots and van Hove autocorrelation function plots.

Acknowledgements

This work was funded through the DOE Office of Science (DE-SC0020282) through the Separations and EPSCoR programs and Energy Efficiency and Renewable Energy Advanced Manufacturing Office. We are grateful to Alabama Supercomputing Center for the computational support.

References

Abedini, A., Ludwig, T., Zhang, Z., Turner, C. H., 2016. Molecular dynamics simulation of bismuth telluride exfoliation mechanisms in different ionic liquid solvents. Langmuir 32, 9982-9992.

Abedini, A., Crabtree, E., Bara, J. E., Turner, C. H., 2017. Molecular simulation of ionic polyimides and composites with ionic liquids as gas-separation membranes. Langmuir 33, 11377-11389.

Abedini, A., Crabtree, E., Bara, J. E., Turner, C. H., 2019. Molecular analysis of selective gas adsorption within composites of ionic polyimides and ionic liquids as gas separation membranes. Chem. Phys. 516, 71-83.

Arce, A., Earle, M. J., Rodríguez, H., Seddon, K. R., 2007. Separation of benzene and hexane by solvent extraction with 1-alkyl-3-methylimidazolium bis {(trifluoromethyl) sulfonyl} amide ionic liquids: effect of the alkyl-substituent length. J. Phys. Chem. B. 111, 4732-4736.

Atkinson, H., Bara, J. E., Turner, C. H., 2020. Molecular-level analysis of the wetting behavior of imidazolium-based ionic liquids on bismuth telluride surfaces. Chem. Eng. Sci. 211, 115270.

Bannan, C. C., Calabró, G., Kyu, D. Y., Mobley, D. L., 2016.Calculating partition coefficients of small molecules in octanol/water and cyclohexane/water. J. Chem. Theory. Comput. 12, 4015-4024.

Bara, J. E., Lessmann, S., Gabriel, C. J., Hatakeyama, E. S., Noble, R. D., Gin, D. L., 2007. Synthesis and performance of polymerizable room-temperature ionic liquids as gas separation membranes. Ind. Eng. Chem. Res. 46(16), 5397-5404.

Bara, J. E., Gabriel, C. J., Hatakeyama, E. S., Carlisle, T. K., Lessmann, S., Noble, R. D., Gin, D. L., 2008. Improving CO_2 selectivity in polymerized room-temperature ionic liquid gas separation membranes through incorporation of polar substituents. J. Mem. Sci. 321(1), 3-7.

Benchea, A., Siu, B., Soltani, M., McCants, J. H., Salter, E. A., Wierzbicki, A., West, K. N., Davis Jr, J. H., 2017. An evaluation of anion suitability for use in ionic liquids with long-term, high-temperature thermal stability. New. J. Chem. 41(16), 7844-7848.

Cassity, C. A., Siu, B., Soltani, M., McGeehee, J. L., Strickland, K. J., Vo, M.,Salter, E. A., Stenson, A.C.,Wierzbicki, A,, West, K. N., Rabideau, B. D., Davis Jr. J.H., 2017. The effect of structural modifications on the thermal stability, melting points and ion interactions for a series of tetraaryl-phosphonium-based mesothermal ionic liquids. Phys. Chem. Chem. Phys. 19, 31560-31571.

Celia-Silva, L. G., Vilela, P., Morgado, P., Lucas, E. F., Martins, L. F., Filipe, E. J., 2020. Pre-aggregation of asphaltenes in presence of natural polymers by molecular dynamics simulation. Energy & Fuels. https://doi.org/10.1021/acs.energyfuels.9b03703.

Chirlian, L. E., Francl, M. M.; 1987. Atomic charges derived from electrostatic potentials: A detailed study. J. Comput. Chem. 8(6), 894-905.

Cichowska-Kopczyńska, I., Joskowska, M., Debski, B., Aranowski, R., Hupka, J., 2018. Separation of toluene from gas phase using supported imidazolium ionic liquid membrane. J. Membrane. Sci., 566, 367-373.

Cui, K., Yethiraj, A., Schmidt, J.R., 2019. Influence of Charge Scaling on the Solvation Properties of Ionic Liquid Solutions. J. Phys. Chem. B., 123(43), 9222-9229.

Darden T., York, D., Pedersen, L., 1993. Particle mesh Ewald: An N·log (N) method for Ewald sums in large systems. J. Chem. Phys. 98,10089-10092.

Domańska, U., Pobudkowska, A., Królikowski, M., 2007 Separation of aromatic hydrocarbons from alkanes using ammonium ionic liquid C2NTf2 at T= 298.15 K. Fluid. Phase. Equilib., 259, 173-179.

Dymond, J. H., Malhotra, R., Isdale, J. D., Glen, N. F., 1988. (p, ϱ, T) of n-heptane, toluene, and oct-1-ene in the range 298 to 373 K and 0.1 to 400 MPa and representation by the Tait equation. J. Chem. Thermodyn. 20, 603-614.

Dymond, J. H., Young, K. J., 1980. Transport properties of nonelectrolyte liquid mixtures—I. Viscosity coefficients for n-alkane mixtures at saturation pressure from 283 to 378 K. Int. J. Thermophys. 1(4), 331-344.

Flowers, B. S., Mittenthal, M. S., Jenkins, A. H., Wallace, D. A., Whitley, J. W., Dennis, G. P.,Wang, M., Turner, C.H., Emel'yanenko, V. N., Verevkin, S.P., Bara, J. E., 2017. 1, 2, 3-Trimethoxypropane: A glycerol-derived physical solvent for CO_2 absorption. ACS Sus. Chem. Eng. 5, 911-921.

Frisch, M. J., Trucks, G. W., Schlegel, H. B., Scuseria, G. E., Robb, M. A., Cheeseman, J. R., et al and Li, X., 2016. Gaussian 16.

Grissom, T. G., Sharp, C. H., Usov, P. M., Troya, D., Morris, A. J., Morris, J. R., 2018. Benzene, toluene, and xylene transport through UiO-66: diffusion rates, energetics, and the role of hydrogen bonding. J. Phys. Chem. C. 122, 16060-16069.

Hess, B., Bekker, H., Berendsen, H. J., Fraaije, J. G., 1997. LINCS: a linear constraint solver for molecular simulations. J. Comput. Chem. 18, 1463-1472.

Hiraga, Y., Sato, Y., Smith Jr, R. L., 2016. Measurement of infinite dilution partition coefficients of isomeric benzene derivatives in [bmim][Tf_2N]-CO2 biphasic system and correlation with the ePC-SAFT equation of state. Fluid. Phase. Equilib. 420, 36-43.

Huang, C., Chen, B., Zhang, J., Liu, Z., Li, Y., 2004. Desulfurization of gasoline by extraction with new ionic liquids. Energy & Fuels 18(6), 1862-1864.

Jorgensen, W. L., Maxwell, D. S., Tirado-Rives, J., 1996, Development and testing of the OPLS all-atom force field on conformational energetics and properties of organic liquids. J. Am. Chem. Soc. 118, 11225-11236.

Kim, E. G., Mattice, W. L., 2002. Radial aspect of local dynamics in polybutadiene melts as studied by molecular dynamics simulation: To hop or not to hop. J. Chem. Phys. 117(5), 2389-2396

Kim, J. H., Lee, S. H., 2002. Molecular dynamics simulation studies of benzene, toluene, and p-xylene in a canonical ensemble. Bullet. Kor. Chem. Soc. 23(3), 441-446.

Köhler, W., Müller, B., 1995. Soret and mass diffusion coefficients of toluene/n-hexane mixtures. J. Chem. Phys. 103(10), 4367-4370.

Larriba, M., Navarro, P., García, J., Rodríguez, F., 2013. Liquid–liquid extraction of toluene from heptane using [emim][DCA],[bmim][DCA], and [emim][TCM] ionic liquids. Ind. Eng. Chem. Res. 52, 2714-2720.

Larriba, M., Navarro, P., García, J., Rodríguez, F., 2014a. Liquid–liquid extraction of BTEX from reformer gasoline using binary mixtures of [4empy][Tf_2N] and [emim][DCA] ionic liquids. Energy & Fuels 28, 6666-6676.

Larriba, M., Navarro, P., García, J., Rodríguez, F., 2014b. Extraction of benzene, ethylbenzene, and xylenes from n-heptane using binary mixtures of [4empy][Tf_2N] and [emim][DCA] ionic liquids. Fluid. Phase. Equilib. 380, 1-10.

Larriba, M., Navarro, P., González, E.J., García, J., Rodríguez, F., 2015. Separation of BTEX from a naphtha feed to ethylene crackers using a binary mixture of [4empy][Tf_2N] and [emim][DCA] ionic liquids. Sep. Purif. Technol. 144, 54-62.

Lindahl, E., Abraham, M.J., Hess, B., van der Spoel, D., 2019. GROMACS 2019.4 Source code (Version 2019.4). Zenodo. http://doi.org/10.5281/zenodo.3460414.

Lísal, M., Chval, Z., Storch, J., Izák, P., 2014. Towards molecular dynamics simulations of chiral room-temperature ionic liquids. J. Mol. Liq. 189, 85-94.

Liu, H., Bara, J. E., Turner, C. H., 2013. DFT study on the effect of exocyclic substituents on the proton affinity of 1-methylimidazole. Chem. Phys. 416, 21-25.

Liu, H., Bara, J. E., Turner, C. H., 2014. Tuning the adsorption interactions of imidazole derivatives with specific metal cations. J. Phys. Chem. A. 118, 3944-3951.

Ludwig, T., Guo, L., McCrary, P., Zhang, Z., Gordon, H., Quan, H., Stanton, M., Frazier, R. M., Rogers, R. D., Turner, C. H., 2015. Mechanism of bismuth telluride exfoliation in an ionic liquid solvent. Langmuir 31, 3644-3652.

Mahurin, S. M., Mamontov, E., Thompson, M. W., Zhang, P., Turner, C. H., Cummings, P. T., Dai, S., 2016. Relationship between pore size and reversible and irreversible immobilization of

ionic liquid electrolytes in porous carbon under applied electric potential. App. Phys. Lett. 109, 143111.

Maton, C., De Vos, N., Stevens, C. V., 2013. Ionic liquid thermal stabilities: decomposition mechanisms and analysis tools. Chem. Soc. Rev. 42, 5963-5977.

Matsumoto, M., Mochiduki, K., Fukunishi, K., Kondo, K., 2004. Extraction of organic acids using imidazolium-based ionic liquids and their toxicity to Lactobacillus rhamnosus. Sep. Purif. Technol. 40, 97-101.

Mulyono, S., Hizaddin, H. F., Alnashef, I. M., Hashim, M. A., Fakeeha, A. H., Hadj-Kali, M. K., 2014. Separation of BTEX aromatics from n-octane using a (tetrabutylammonium bromide+ sulfolane) deep eutectic solvent–experiments and COSMO-RS prediction. RSC. Adv. 4(34), 17597-17606.

Odugbesi, G. A., Nan, H., Soltani, M., Davis Jr, J. H., Anderson, J. L., 2019. Ultra-high thermal stability perarylated ionic liquids as gas chromatographic stationary phases for the selective separation of polyaromatic hydrocarbons and polychlorinated biphenyls. J. Chromatogr. A 1604, 460466.

Patel, S. A., Brooks III, C. L., 2006. Revisiting the hexane-water interface via molecular dynamics simulations using nonadditive alkane-water potentials. J. Chem. Phys. 124(20), 204706.

Pena-Pereira, F., Namieśnik, J., 2014. Ionic liquids and deep eutectic mixtures: sustainable solvents for extraction processes. Chem. Sus. Chem 7, 1784-1800.

Rabideau, B. D., West, K. N., Davis, J. H. 2018. Making good on a promise: ionic liquids with genuinely high degrees of thermal stability. Chem. Commun. 54, 5019-5031.

Sappidi, P., Namsani, S., Ali, S. M., Singh, J. K., 2018. Extraction of Gd^{3+} and UO_2^{2+} Ions Using Polystyrene Grafted Dibenzo Crown Ether (DB18C6) with Octanol and Nitrobenzene: A Molecular Dynamics Study. J. Phys. Chem. B. 122, 1334-1344.

Shirts, M. R., Pitera, J. W., Swope, W. C., Pande, V. S., 2003. Extremely precise free energy calculations of amino acid side chain analogs: Comparison of common molecular mechanics force fields for proteins. J. Chem. Phys. 119, 5740-5761.

Shannon, M. S., Irvin, A. C., Liu, H., Moon, J. D., Hindman, M. S., Turner, C. H., Bara, J. E., 2015. Chemical and physical absorption of SO_2 by N-functionalized imidazoles: experimental results and molecular-level insight. Ind. Eng. Chem. Res. 54, 462-471.

Stephens, P. J., Devlin, F. J., Chabalowski, C. F. N., Frisch, M. J., 1994. Ab initio calculation of vibrational absorption and circular dichroism spectra using density functional force fields. J. Phys. Chem. 98, 11623-11627.

Słomińska, M., Król, S., Namieśnik, J., 2013. Removal of BTEX compounds from waste gases, destruction and recovery techniques. Crit. Rev. Env. Sci. Tec. 43, 1417-1445.

Szala-Bilnik, J., Abedini, A., Crabtree, E., Bara, J. E., Turner, C. H., 2019. Molecular Transport Behavior of CO_2 in Ionic Polyimides and Ionic Liquid Composite Membrane Materials. J. Phys. Chem. B. 123(34), 7455-7463.

Szala-Bilnik, J., Crabtree, E., Abedini, A., Bara, J. E., Turner, C. H., 2020. Solubility and diffusivity of CO_2 in ionic polyimides with $[C(CN)_3]_x[oAc]_{1-x}$ anion composition. Comput. Mater. Sci. 174, 109468.

Wu, R., Deng, M., Kong, B., Wang, Y., Yang, X., 2009. Molecular dynamics simulations of ammonium surfactant monolayers at the heptane/water interface J. Phys. Chem. B. 113(38), 12680-12686.

Zhang, J., Huang, C., Chen, B., Ren, P., Lei, Z., 2007. Extraction of aromatic hydrocarbons from aromatic/aliphatic mixtures using chloroaluminate room-temperature ionic liquids as extractants. Energy & Fuels 21, 1724-1730.

Zhang, Y., Maginn, E. J., 2015. Direct correlation between ionic liquid transport properties and ion pair lifetimes: A molecular dynamics study. J. Phys. Chem. Lett, 6(4),700-705.